Ionics (2025) 31:3559–3573
https://doi.org/10.1007/s11581-025-06118-2

RESEARCH

Sustainable coconut shell charcoal counter electrodes for efficiency enhancement in CdS quantum dot solar cells

M. A. K. L. Dissanayake[1,2] · A. K. Karunaratne[1,2] · G. K. R. Senadeera[1,3] · T. M. W. J. Bandara[2,4] · G. R. A. Kumara[1] · A. D. T. Medagedara[1] · J. M. K. W. Kumari[1] · I. Albinsson[5] · B.-E. Mellander[6] · M. Furlani[6] · N. B. Chaure[7] · O. I. Olusola[8]

Received: 16 October 2024 / Revised: 31 December 2024 / Accepted: 26 January 2025 / Published online: 5 February 2025

Abstract

The use of activated coconut shell charcoal (ACSC) was explored as a cost-effective and viable alternative to platinum (Pt) counter electrodes (CE) in CdS quantum dot–sensitized solar cells (QDSSCs). The photovoltaic performances of QDSSCs with newly fabricated ACSC CEs by spraying method and Pt CEs were evaluated using current density–voltage measurements under 100 $mWcm^{-2}$ light illumination. While the QDSSC with a Pt CE showed an efficiency of 1.26%, the QDSSC with an ACSC CE, with an optimal thickness of 25 µm, corresponding to a spray time of 60 s, showed an efficiency of 2.93%, demonstrating a more than two-fold increase in the efficiency. The physicochemical parameters of ACSC CEs were analyzed using FTIR, Raman, X-ray diffraction, cyclic voltammetry (CV), and Tafel characterization. CV, Tafel, and electrochemical impedance (EIS) analysis confirmed the superior electrocatalytic activity of the ACSC CE compared to the Pt CE for QDSSCs. The efficiency enhancement can be attributed to the increased photocurrent density due to the superior electrocatalytic activity of ACSC, which promotes efficient polysulfide reduction at the electrolyte/counter electrode interface. The porous nature of ACSC provides an increased specific surface area, facilitating redox reactions and improving the interaction between the electrolyte and the counter electrode. Additionally, the enhanced charge transfer capabilities of the ACSC-based counter electrode contribute to efficient electron transport and reduced recombination losses. These properties collectively optimize the cell's performance by ensuring effective energy conversion. Consequently, ACSC is emerging as a promising novel material for counter electrodes in QDSSCs.

Keywords CdS quantum dot–sensitized solar cells · Counter electrodes · Activated coconut shell charcoal · Efficiency enhancement

Introduction

Since 1989, when Burnham and Diggan conducted their initial study on quantum dot–sensitized solar cells (QDSSC) [1], scientists have gained increasing attention on using these solar cells in the renewable energy sector. The interest stems from the exceptional properties of quantum dots (QDs), which include a strong response to visible light photons, tunable bandgaps, and optical properties by controlling size, as well as their ability of multiple exciton generation (MEG) [2]. The typical structure of a QDSSC has a QD-sensitized semiconducting photoanode, usually a thin film of TiO_2, and a counter electrode sandwiched with an electrolyte containing a sulfide-based redox couple. The nanostructure of TiO_2 plays a significant role in the performance of QDSSCs, as it acts as a suitable electron transport layer, ensuring efficient charge separation and collection. Among the quantum dots available, CdS has received a great deal of attention due to its bandgap of 2.42 eV, which lies in the visible spectrum. In addition, the position of the energy level of the conduction band of the CdS is slightly higher than that of the TiO_2, thus enhancing the electron transfer from the CdS to TiO_2. Among the different deposition methods available for fabricating QDs, the sequential ionic layer adsorption and reaction or the SILAR method has emerged as a promising method used for the deposition of semiconductor quantum dots because of its effectiveness and lower cost compared to other techniques. The SILAR method involves repeated cycles of dipping a substrate into cationic and anionic precursor solutions, separated by rinse steps to prevent cross-contamination. Each cycle adds an atomic or molecular layer to the film, enabling precise control over the CdS film

Extended author information available on the last page of the article

thickness and composition. The composition and the concentration of the precursor solution have a close relationship with the nature of the QDs, and by adjusting the deposition cycles, the SILAR approach allows us to regulate the loading quantity and the crystallite sizes of CdS QDs. Because of the quantum confinement effect of the QDs, hot electrons can be used to produce numerous electron–hole pairs by the impact ionization effect. This allows one to modify the optical characteristics and the band gap of a QD by simply varying its size. The high value of the extinction coefficient of QD sensitizers, which is expected to lower the dark current and raise a solar cell's overall efficiency, is another advantage over traditional dyes which are used to sensitize the photoanode in dye-sensitized solar cells (DSSCs). However, compared to traditional Ru dye-based DSSCs, comparatively fewer investigations have been reported on QDSSCs to date, and the reported efficiencies are still very low and far from commercialization of these devices.

Normally, the QDSSCs operating under concentrated sunlight can have a maximum theoretical conversion efficiency of up to 66% [2]. In practice, however, certified power conversion efficiency (PCE) values for QDSSCs have improved from 5 to 14.4% over the past several years [3] with various modifications applied to these QDs and devices. However, the efficiencies still remain low in QDSSCs fabricated with a single type of quantum dots (QDs). The recent impressive advancements in engineering photoanodes for enhanced efficiencies in these QDSSCs have simulated revisiting the other major component of the solar cell, namely the counter electrode.

To achieve higher efficiencies in QDSSCs, the CE must satisfy several conditions. The CE should have a high electrocatalytic activity to effectively catalyze the reduction of polysulfide species to the polysulfide anions. It should be photostable and chemically compatible with the polysulfide electrolyte without dissolving in it. The work function of the CE should be in the range of 4.3–5.3 eV. Additionally, it should be non-toxic, inexpensive, and abundant [4]. Some materials that fulfill these criteria include metal sulfides such as NiS, CoS, and CuS [5] and conducting polymers such as poly(pyrrole), polythiophene (PT), and poly(3,4-ethylenedioxythiophene) (PEDOT) [6]. Moreover, noble metals such as Pt and Au [7] and graphite nanostructures such as reduced graphene oxide and multi-walled carbon nanotubes [8–10] have been successfully employed as CEs in QDSSCs. Among these materials, Pt has been extensively used as the CE in QDSSCs. Most Pt-based CEs are prepared by electrochemical deposition or sputtering of platinum. These methods are expensive, and the fabrication processes are highly energy-consuming. Moreover, Pt is an expensive noble metal, which limits the large-scale commercial application of QDSSCs. Even though Pt is commonly used, it also has some drawbacks as a CE in QDSSCs with sulfide-based electrolytes, such as chemical adsorption and corrosion of the Pt electrode [11]. Therefore, exploring alternative substitutes for Pt is crucial. One of the most viable and low-cost approaches is to replace Pt with abundant, non-precious materials such as graphite, graphite-based materials, or other carbon-based materials [7].

Carbon-based materials, including graphite, graphite-based composites, and activated coconut shell charcoal (ACSC), have garnered significant attention as sustainable and cost-effective alternatives to traditional electrode materials in electrochemical power sources. These materials offer exceptional properties such as high electrical conductivity, high electrocatalytic activity, chemical stability, and tunable porosity, making them suitable for applications in batteries, supercapacitors, and dye-sensitized solar cells (DSSCs). Graphite and its derivatives, such as graphene, provide excellent electron transport capabilities and structural integrity, enabling high performance in energy storage and conversion systems. Similarly, ACSC, derived from renewable coconut shells, combines a high specific surface area with superior electrocatalytic activity and electrical conductivity, ensuring efficient charge transfer and enhanced energy efficiency. Together, these carbon-based materials hold immense potential for advancing sustainable energy technologies while addressing the cost and scalability challenges of conventional electrode materials.

The rising demand for cost-effective and sustainable materials in electrochemical applications has driven significant research into alternatives to platinum, a commonly used but expensive and scarce material. Activated coconut shell charcoal (ACSC) has emerged as a promising candidate due to its unique properties, including high specific surface area, excellent electrical conductivity, and superior electrocatalytic activity. These characteristics make ACSC an attractive material for various applications such as fuel cells, dye-sensitized solar cells (DSSCs), supercapacitors, and batteries.

ACSC is derived from an abundant and renewable agricultural byproduct, coconut shells, making it an environmentally friendly and economically viable option. Through activation processes, the surface area and porosity of the material are significantly enhanced, providing more active sites for electrochemical reactions. Additionally, its high electrical conductivity ensures efficient electron transport, a critical requirement for electrodes in energy conversion and storage devices. Studies have demonstrated that carbon-based materials, including ACSC, exhibit competitive catalytic performance in reactions such as the oxygen reduction reaction (ORR), a key process in fuel cells, and the iodide/triiodide redox reaction in DSSCs, thus presenting a viable alternative to platinum [7, 12–14].

Furthermore, the cost of producing ACSC is substantially lower than that of platinum, and its utilization aligns with

global efforts to reduce reliance on critical raw materials. By leveraging the intrinsic properties of ACSC, researchers aim to develop high-performance, low-cost electrochemical systems that support the transition to sustainable energy technologies. This paper investigates the potential of ACSC as a substitute for platinum, focusing on its electrocatalytic performance, structural characteristics, and practical applications in electrochemical systems.

Among carbon-based materials, activated charcoal (AC) mainly comprises carbon atoms arranged in aromatic sheets that are randomly cross-linked. Additionally, it may contain heteroatoms such as oxygen, nitrogen, sulfur, or hydrogen, depending on the raw material used and the physical or chemical treatments applied. The irregular arrangement of these aromatic sheets creates a solid structure with free spaces between them.

Any carbonaceous material with a high carbon concentration, whether of animal, plant, or mineral origin, can be converted into activated charcoal. Common raw materials used for manufacturing activated charcoal include wood, charcoal, nutshells, bone, and synthetic polymers like polyvinyl chloride (PVC). It has been reported that the highest-quality AC can be derived from coconut shells and apricot pits [15]. AC is typically produced through two primary processes: physical or gas activation and chemical activation. The selection of the activation method depends on the starting material and the desired carbon density, whether granular or powdered. In the chemical process, both carbonization and activation occur simultaneously.

This study illustrates the potential of using low-cost, sustainable materials, such as activated coconut shell charcoal, to create effective counter electrodes for QDSSCs. This approach not only offers a cost-effective and eco-friendly alternative to traditional platinum electrodes but also improves the overall performance and sustainability of solar energy conversion. The reported efficiency of 2.98% in this study highlights the potential of using ACSC to reduce the cost of solar energy conversion, while utilizing abundant and environmentally sustainable resources.

Materials and methods

Materials

Activated coconut shell charcoal (ACSC), polyvinylpyrrolidone (BDH, England), and isopropanol were used as the initial materials to prepare the counter electrodes. For the TiO_2 photoanodes, fluorine-doped tin oxide (FTO) conducting glass substrates (8 Ωcm^{-2}, Solaronix), titanium dioxide P90 powder (Evonik, Germany), titanium dioxide P25 powder (Degussa), polyethylene glycol (99.8%, Sigma-Aldrich), Triton X-100 (Sigma-Aldrich), and cadmium(II) chloride (99.99%, Sigma-Aldrich) were utilized as received without further purification. Additionally, potassium chloride (99%, BDH), sodium sulfide hydrate ($\geq 60\%$, Sigma-Aldrich), and sulfur were used as received to prepare the polysulfide electrolyte.

Preparation of the photo-anode

FTO plates (1 cm × 2 cm) were cleaned according to the standard procedure [16]. To deposit the less porous, compact TiO_2 films on the FTO substrates, a paste was prepared by mixing 0.25 g of TiO_2 P90 powder with 1 mL of 0.1 M HNO_3 and grinding it until a creamy consistency was achieved. This paste was then applied to the conducting side of the FTO glass using spin coating at 3000 rpm for 1 min. The electrodes were subsequently sintered at 450 °C for 45 min and then cooled to room temperature.

To fabricate the porous second TiO_2 layer, 0.25 g of TiO_2 P25 powder was ground with 1.0 ml of 0.1 M HNO_3. Then, 0.02 g of Triton X-100 surfactant was added to prevent the aggregation of TiO_2 particles [17]. Finally, 0.05 g of PEG 2000 was incorporated into the paste, and the mixture was ground until it reached a creamy consistency. The P25 layer was then applied on top of the previously prepared P90 layer using the "doctor blade" method. The FTO/TiO_2 P90/TiO_2 P25 electrodes were sintered at 450 °C for 45 min, after which they were allowed to cool gradually. The effective area of all QDSSCs was adjusted to 0.25 cm^2 by removing any excess material.

Deposition of CdS quantum dots

The CdS quantum dots (QDs) were grown on the previously prepared TiO_2 electrodes using the SILAR method. Aqueous solutions of 0.1 M $CdCl_2$ and 0.1 M Na_2S were used as the cationic and anionic precursor solutions, respectively. The mesoporous TiO_2 electrode was first immersed in the cationic solution, allowing cadmium(II) ions to adsorb onto the substrate's surface. To remove any unabsorbed ions, the substrate was rinsed with distilled water for 10 s. Next, the substrate was dipped in the anionic precursor solution, where sulfur ions react with the adsorbed cadmium ions. Afterward, the substrate was again rinsed with distilled water for 10 s to remove loosely bound ions, completing one SILAR cycle for CdS QD deposition. The dipping time for each precursor solution was kept constant at 1 min. The size of the CdS QDs is determined by the concentration of the precursor solutions, dipping duration, and the number of SILAR cycles [18]. In this study, the quantum dot size was controlled by adjusting the number of SILAR cycles while fixing the other parameters constant.

Preparation of activated coconut shell charcoal (ACSC)-based counter electrodes

The preparation of ACSC was carried out following the method outlined by Medagedara et al. in 2022 [19]. In brief, cleaned coconut shells were combusted in a metal chamber until the flames, produced by the volatile materials, became incandescent. Once the shells were sufficiently burned, they were immersed in distilled water to quench them. After quenching, the coconut shells were heated in a box furnace at 900 °C for 20 min. The hot charcoal was then transferred to a tank containing distilled water for cooling. Finally, after removing the cooled charcoal from the tank, it was dried and ground into a fine powder [19].

The ACSC suspension was prepared by combining 0.5 g of ACSC powder, 0.05 g of polyvinylpyrrolidone (PVP), and 8.0 ml of isopropanol (IPA). This mixture was ground in an agate mortar for 10 min and then ultrasonicated for 10–15 min. The resulting dispersion was sprayed onto a cleaned FTO glass, covering a 1.0 cm × 2.0 cm area, using a spray gun as described in the reference [20], while the glass was placed on a hot plate set at 150 °C. The ACSC-coated glass was subsequently sintered in air at 350 °C in a furnace for 20 min.

Preparation of the solution electrolyte

To fabricate the QDSSCs, an electrolyte solution was used with either Pt or ACSC as the counter electrode. The polysulfide electrolyte solution was prepared as follows: sulfur (2 M), 2 M Na_2S, and 0.2 M KCl were dissolved in a 3:7 (v/v) mixture of deionized water and methanol. This mixture was stirred continuously for 3 h before being used as the electrolyte in QDSSCs.

Characterization

For the structural characterization of the prepared ACSC counter electrode, Fourier transform infrared (FTIR) spectra were recorded using a Bruker Alpha FTIR spectrometer, covering the wavelength range from 400 to 4000 cm^{-1}. The X-ray diffraction (XRD) pattern of the ACSC powder was obtained with the Bruker D8 advanced eco X-ray diffraction system, where data were collected with a step interval of 0.2° in the 2θ range of 5 to 80°. Raman spectroscopic measurements were performed in order to evaluate the crystallinity, graphitization, and the degree of disorder of the ACSC electrode. For the morphological characterization of the ACSC counter electrode surface, as well as for determining the thickness of the counter electrode, scanning electron microscopy (SEM, Zeiss) was used. Each QDSSC was characterized by current–voltage measurements under 100 mW cm^{-2} illumination, using an AM 1.5 spectral filter and a Keithley 2400 computer-controlled multimeter, with an effective cell area of 0.25 cm^2. Incident photon to current efficiency energy (IPCE) measurements were carried out with an experimental setup involving monochromatic light illumination from a Bentham PVE 300 unit, equipped with a TMC 300 monochromator-based system and a 150-W xenon arc lamp, covering wavelengths from 300 to 1100 nm. A calibrated Si photodetector (type DH) was used as the reference.

Electrochemical impedance spectroscopy (EIS) measurements were conducted using a Metrohom Autolab potentiostat/galvanostat (Metrohm Autolab PGSTAT 128N) equipped with an FRA 32 M module, covering the frequency range from 0.01 Hz to 1 MHz. Nyquist plots of each QDSSC were analyzed by fitting the data to an equivalent circuit model using NOVA 1.11 software, and the EIS parameters of ACSC and Pt counter electrodes (CEs) were determined and compared. To study and compare the electrochemical behavior of ACSC and Pt CEs, cyclic voltammetry (CV) measurements, EIS analysis, and Tafel analysis were performed. Cyclic voltammograms of both CE types were recorded in a polysulfide-based liquid electrolyte at a scan rate of 20 mV s^{-1}, with a sweep potential ranging from − 1.0 to + 1.0 V. The Ag/AgCl electrode served as the reference, while a Pt rod was used as the counter electrode. ACSC and sputtered Pt CEs were used as working electrodes, each with an active area of 1.00 cm^2. EIS and Tafel analyses were conducted on the two counter electrodes separately using symmetrical dummy cells, which were constructed with two identical electrodes, each having an active area of 1.00 cm^2, to investigate the charge transfer process at the CE/electrolyte interface. These tests were performed in the dark using the same Metrohom Autolab potentiostat/galvanostat (Metrohm Autolab PGSTAT 128N).

Results and discussion

Structural analysis

The FTIR spectra of ACSC, as shown in Fig. 1, reveal notable structural characteristics. The broad absorption band at 3433 cm^{-1} is associated with the stretching vibration of the OH functional group [21]. Additionally, a distinct absorption band at 1642 cm^{-1} corresponds to N–H bending vibrations, which is typical of mesoporous activated charcoal [21]. Smaller peaks are also observed at 1392 cm^{-1} and 1119 cm^{-1}. The peak at 1392 cm^{-1} is attributed to C-O stretching, while the peak at 1119 cm^{-1} corresponds to C-H wagging [21]. The FTIR data obtained in this study closely align with results from other research groups, further confirming the presence of ACSC [22].

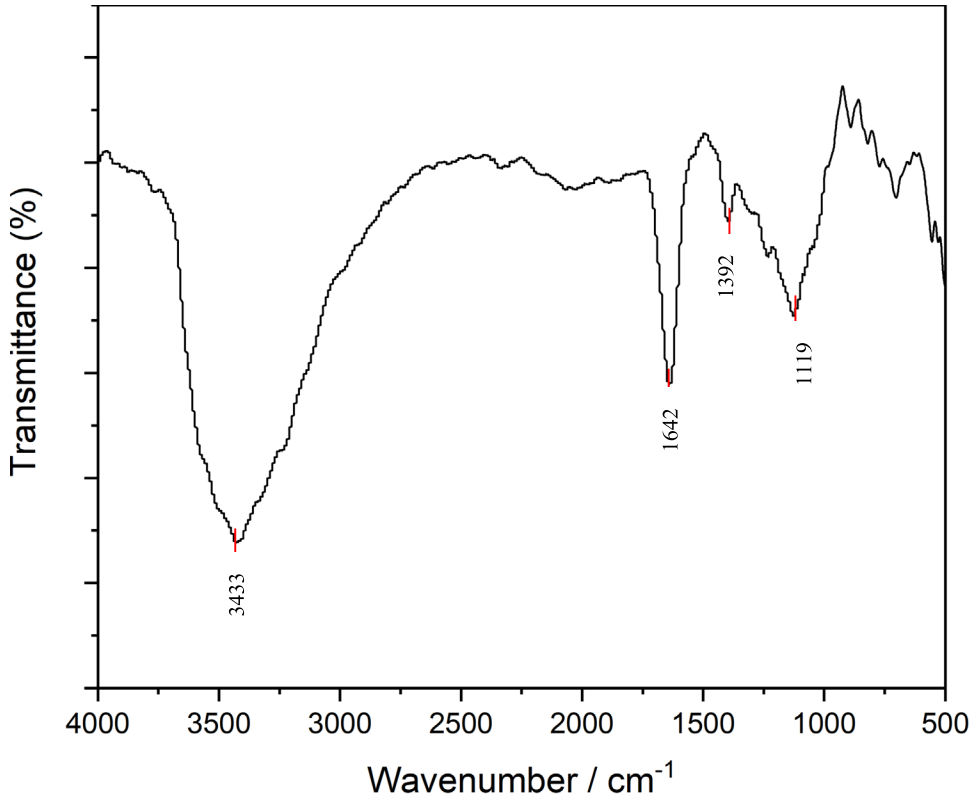

Fig. 1 FTIR spectrum of ACSC powder

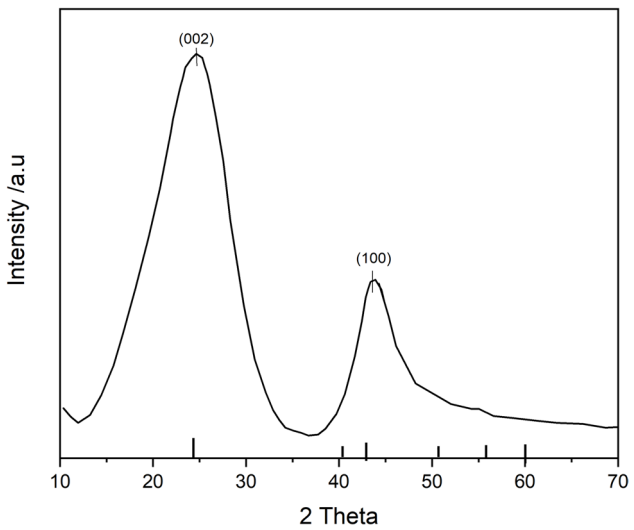

Fig. 2 X-ray diffractogram of activated coconut shell charcoal

Figure 2 shows the XRD pattern of ACSC powder. The broad peaks centered at $2\theta = 24.65°$, and $2\theta = 43.91°$ indicate the poor crystallinity of the material with large crystallite sizes 87.12 nm along the (002) direction and 176.84 nm along the (101) direction (JCPDS 00–056–0159) [13, 23]. A similar XRD pattern has been observed for activated charcoal derived from orange peel [24]. Since the (200) diffractions of graphite also appear in this region, the band centered at $2\theta = 25°$ can be attributed to the graphitic structure of the sample [12].

Figure 3 shows the Raman spectrum pattern of ACSC powder. This was conducted to evaluate the crystallinity, graphitization, and the degree of disorder of the ACSC. The Raman spectrum revealed the characteristic D-band at 1343 cm^{-1} and G-band at 1601 cm^{-1}, with an intensity ratio (I_D/I_G) of 1.49. Compared with the values reported in the literature for the carbonesium materials such as graphite and graphite flakes, this value seems to be high [25]. Several factors contribute to this high value, including the formation of structural defects, the enhancement of edge planes, intercalation effects, and surface modifications during the activation process of the charcoal. Together, these factors result in a material with a higher degree of disorder, which is beneficial for electrocatalytic activity by increasing the availability of active sites for redox reactions in QDSSCs [26]. Additionally, the 2D-band at 2898 cm^{-1} suggests the presence of graphitic stacking. The crystallite size was calculated using the Tuinstra-Koening equation given in the Eq. 1,

$$L_a = \frac{C}{(\frac{I_D}{I_G} - 1)} \quad (1)$$

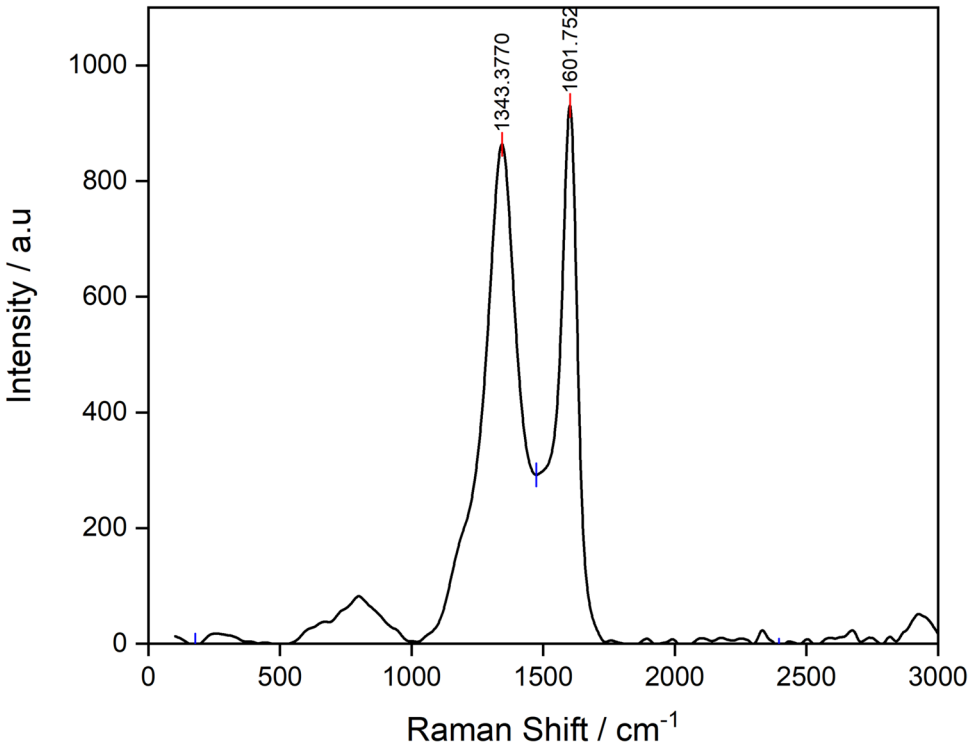

Fig. 3 Raman spectrum of ACSC powder

where, L_a is the crystallite size, I_D/I_G is the intensity ratio of the D-band to G-band, and C is the constant typically around 4.4 for graphite-like materials. The crystallite size was calculated to be 8.97 nm, confirming the graphitic nature of the material.

Morphological analysis of ACSC-based CE

Figure 4a and b present the SEM images of ACSC counter electrodes. These images indicate that the ACSC thin films exhibit a spongy-like structure, resembling the SEM images reported by Kumarasinghe et al. [12]. The aggregated particle sizes are estimated to range between 2 and 6 µm. As depicted in Fig. 4b, the thickness of the ACSC-based CE, which corresponds to the best-performing solar cell is approximately 25 µm. This optimum thickness was achieved by varying the spray durations (5 s, 15 s, 30 s, 60 s, 90 s, 120 s), while maintaining a constant distance between the spray gun and the cell, as described by Dissanayake et al. [20]. In our previous studies, EDX measurements confirmed that, aside from carbon (C) and oxygen (O), no other elements were present in the ACSC [12]. Furthermore, the atomic percentages of C and O were approximately 89% and 11%, respectively, suggesting the presence of oxygen-containing functionalities attached to at least ten carbon atoms. These findings are in strong agreement with FTIR measurements, which indicated the presence of –OH, –COOH, and other functional groups in the ACSC.

Photovoltaic performance of QDSSCs

The current density–voltage (J-V) characteristics of the QDSSCs with different CEs were examined under the light irradiation of 100 mW cm^{-2}. Figure 5 presents the J-V curves of QDSSCs based on ACSC CEs, varying in thickness according to different spraying times used during fabrication. The photovoltaic parameters derived from Fig. 5 are listed in Table 1. For consistency, the number of FTO plates and the solution composition were kept constant throughout the experiments and all the measurements were repeated at least five times with new cells. The highest efficiency, 2.93%, was achieved in QDSSCs with ACSC CEs sprayed for 60 s. As the ACSC layer's thickness increased, a significant reduction in short-circuit current density (J_{SC}) and overall efficiency was observed.

The experimentally observed maximum in the photocurrent in a QDSSC made with a TiO_2 photoanode, liquid redox couple, and a nanoporous ACSC CE can be explained by considering the interplay between the electrocatalytic effect and the electron transport resistance of it. The electrocatalytic effect of the CE plays a crucial role in facilitating the redox reactions of the liquid electrolyte, such as the $S^{2-}{}_n$ / S^{2-} redox couple. The efficiency of this process depends on the electrocatalytic activity, which is directly influenced by the number of active sites available for these reactions. An

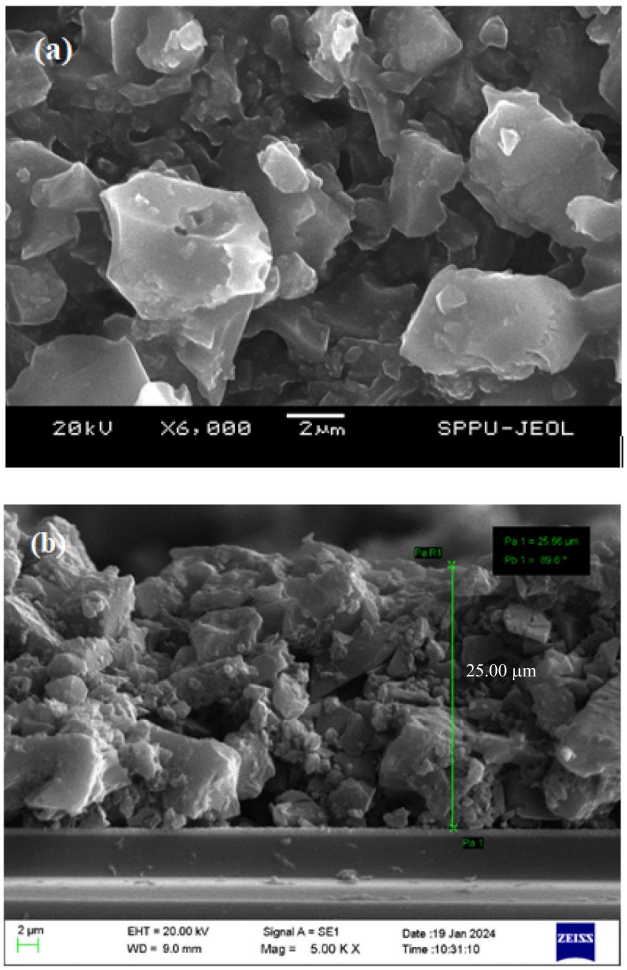

Fig. 4 SEM images of **a** surface of the ACSC counter electrode and **b** cross section of ACSC counter electrode

increase in the thickness of the counter electrode enhances its surface area, thereby providing more active sites. This improvement in the electrocatalytic activity accelerates the redox reaction rate, ensuring efficient regeneration of the oxidized dye and contributing to higher photocurrent generation in the system. On the other hand, the mechanism of electron transport in QDSSCs involves electrons generated in the external circuit traversing the CE reactions. As the CE thickness increases, resistance to electron transport rises due to the longer travel distance and the porous nature of the material. This increased resistance beyond a certain thickness impedes efficient electron transport, leading to energy losses and a decline in photocurrent. At low CE thickness, the number of active sites is insufficient for optimal redox reactions, which limits the photocurrent despite low resistance. As thickness increases, more active sites become available, enhancing the redox reaction rate and the photocurrent. The maximum photocurrent is achieved at an optimal thickness where a balance exists between sufficient active sites and manageable resistance. Beyond this point, further increases in thickness result in excessive resistance, reducing the photocurrent despite the presence of additional active sites. This observed maximum arises from the interplay between the increasing electrocatalytic effect, which enhances photocurrent, and the rising electron transport resistance, which hinders it. Thus, optimizing CE thickness is critical for achieving peak performance in QDSSCs [27].

Figure 6 illustrates the *J-V* curves for QDSSCs fabricated with conventional Pt and ACSC CE with optimized thickness. The photovoltaic parameters obtained from these QDSSCs are presented in Table 2. Through multiple reproducible trials, the quantum dot–sensitized solar cells (QDSSCs) fabricated with ACSC CEs showed a consistently high power conversion efficiency (PCE) of 2.93%, accompanied by a short-circuit current density (*s.*

In contrast, the Pt CE exhibited lower values of 1.23% for PCE and 7.34 mA cm^{-2} for J_{sc}. This discrepancy can be attributed to the incompatibility of platinum with the polysulfide electrolytes, likely caused by corrosion, which negatively affects the device's stability and durability, leading to reduced values for PCE, J_{sc}, and fill factor [28]. The adsorption of sulfur atoms on the surface of the Pt electrode affects negatively in its electrocatalytic activity and conductivity, hindering the regeneration of the sulfide electrolyte. This results in increased series resistance, limiting the performance of the QDSSC [29]. The enhanced photovoltaic performance of ACSC CE-based QDSSCs can be attributed to the improved retention of the liquid electrolyte within the porous structure and the increased availability of active sites for the redox reactions of the polysulfide electrolyte, facilitated by the larger effective surface area of the ACSC CE.

As noted by all performance of QDSSCs [30–32].

Figure 7 displays the IPCE spectra for QDSSCs fabricated with ACSC and Pt counter electrodes. The data clearly indicate that within the 400–500 nm wavelength range, the ACSC-based counter electrode yields a higher IPCE than the cell with the Pt-based counter electrode. The observed increase in J_{sc} in the device with the ACSC counter electrode (CE), relative to the device with the Pt CE, is further substantiated by the larger integrated area under the curve in the corresponding incident photon-to-current efficiency (IPCE) spectrum.

Electrochemical impedance spectroscopy (EIS) analysis of QDSSCs

EIS measurements were conducted to investigate the interfacial transfer processes in QDSSCs made with both ACSC-based and Pt-based counter electrodes. Figure 8 presents the Nyquist plots for QDSSCs fabricated with (1) an ACSC counter electrode and (2) a Pt counter electrode. The smaller semicircle observed in

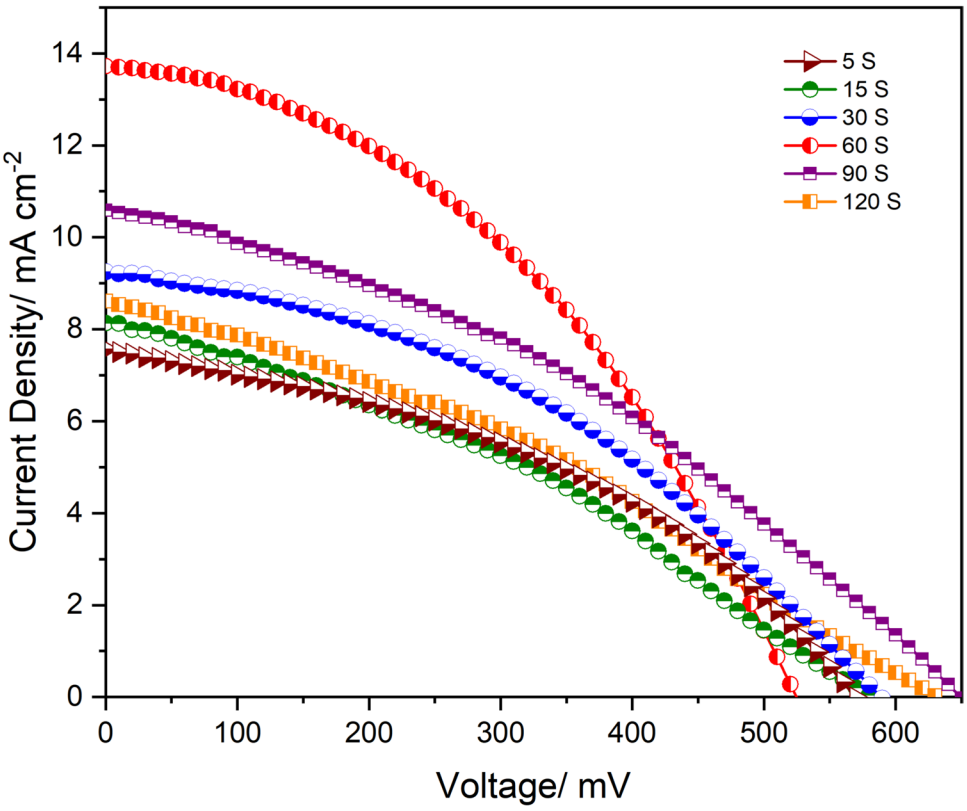

Fig. 5 Current density vs. photovoltage (J_{sc} vs V_{oc}) characteristics of QDSSCs made with ACSC CEs with different thicknesses prepared using different spraying times

Table 1 Photovoltaic performance of QDSSCs with ACSC CEs fabricated using varying spray durations

Spraying time/S	J_{SC}/mAcm^{-2}	V_{OC}/mV	FF %	Efficiency %
5	7.50	582	36.7	1.60
15	8.10	569	37.6	1.73
30	9.30	588	39.5	2.16
60	13.62	513	41.9	2.93
90	10.51	649	36.0	2.46
120	8.51	631	33.9	1.82

the high-frequency region is associated with the electrochemical resistance at the photoanode/electrolyte interface ($R2_{CT}$). In contrast, the larger semicircle corresponds to the charge transfer resistance at the counter electrode/electrolyte interface ($R1_{CT}$). The series resistance (R_S) is linked to the recombination of charge transfer resistance at the FTO/TiO_2 interface as well as the resistance of the external circuit [33]. The charge transfer resistance values were determined by fitting the impedance parameters to an equivalent circuit model, as illustrated in the inset of Fig. 8, using NOVA software. All the EIS parameters obtained from the equivalent circuit are listed in Table 3. The parameter $R1_{CT}$ is linked to electrocatalytic activity, where a lower $R1_{CT}$ indicates

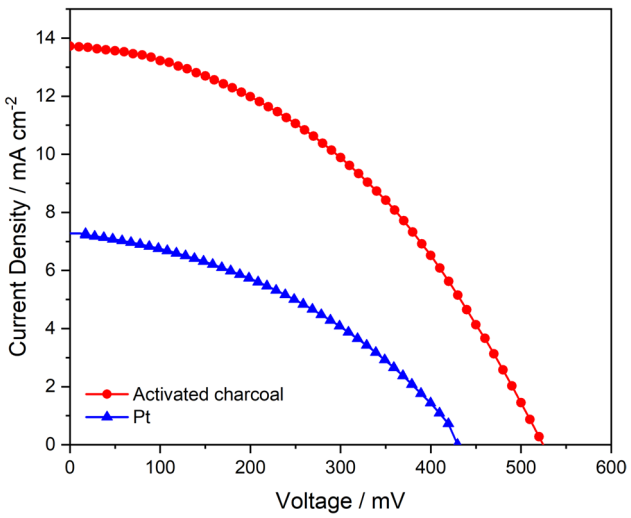

Fig. 6 Current density–voltage characteristics of QDSSCs made with (a) Pt (lower curve) and (b) optimized ACSC (upper curve) CEs

Table 2 Photovoltaic parameters of QDSSCs made with Pt and ACSC CEs

CE composition	J_{SC}/mAcm^{-2}	V_{OC}/mV	FF %	Efficiency %
Pt	7.34	429.0	39.1	1.23
ACSC	13.62	513.0	41.9	2.93

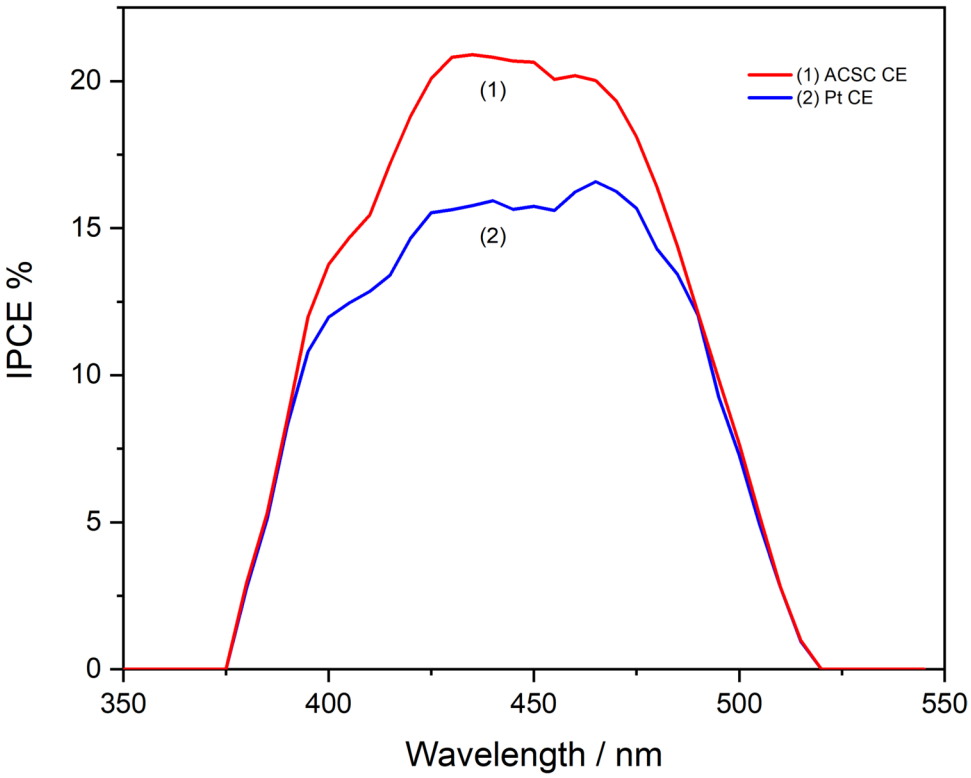

Fig. 7 IPCE spectra of the QDSSCs fabricated with (1) ACSC-based CE and (2) Pt-based CE

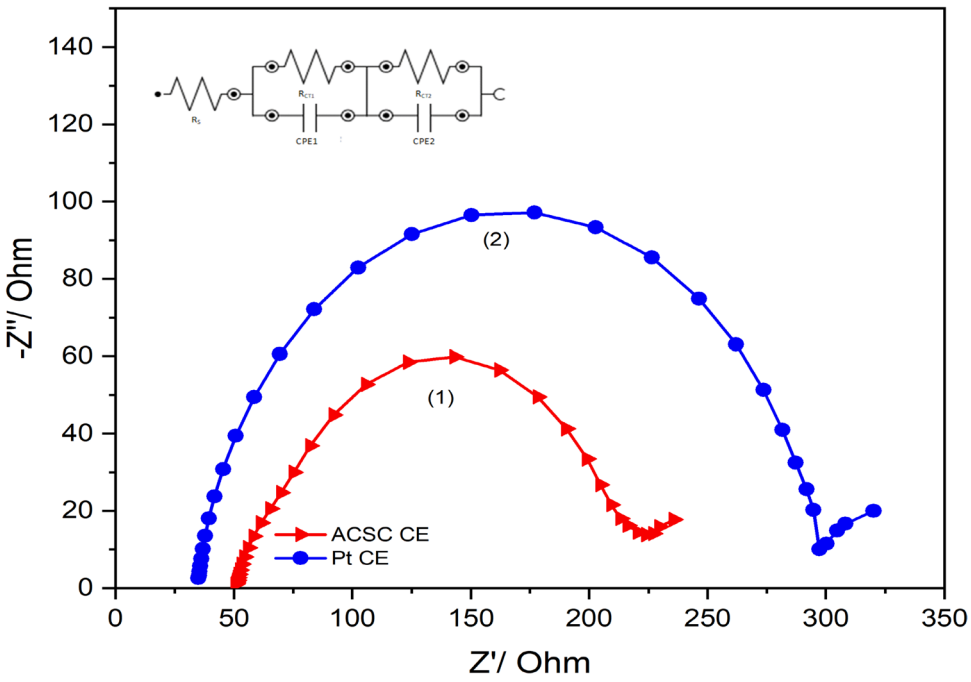

Fig. 8 Nyquist plots of DSSCs with (1) ACSC-based counter electrode and (2) Pt counter electrode

Table 3 Electrochemical parameters of QDSCs with the two different counter electrodes extracted from EIS data as shown in Fig. 7

CE	R_s (Ω)	$R1_{CT}$ (Ω)	$R2_{CT}$ (Ω)
Pt	34.36	205.84	93.85
ACSC	49.88	123.02	14.79

greater electrocatalytic activity for the polysulfide electrolyte [33]. Higher electrocatalytic activity of ACSC CE enhances the kinetics of the redox reactions involving the polysulfide electrolyte, resulting in a lower $R1_{CT}$ compared to Pt. Another reason is the structural defects and heteroatoms such as oxygen present in ACSC improve

the electron transfer rates by serving as additional catalytic sites. This higher surface area and defect-rich structure promote faster charge transfer between the electrolyte and the photoanode, thereby reducing the value of $R2_{CT}$ [34]. Similarly, a lower R_S would correspond to the higher electrical conductivity of the ACSC CE and an improved fill factor [35].

Therefore, the lower $R1_{CT}$ value of 123.02 Ω for the ACSC counter electrode, compared to the Pt counter electrode, reflects the superior electrocatalytic activity of the ACSC CE.

Cyclic voltammetry (CV) analysis

The results of the CV measurements are presented in Fig. 9a. In the CV curve, a more negative potential indicates reduction, while a positive potential signifies the oxidation of the polysulfide electrolyte [36, 37]. The catalytic performance of the CEs is quantitatively evaluated by measuring the peak current densities (J_{ox} and J_{red}) and the peak-to-peak separation (ΔE_p) between the reduction and oxidation peaks of the redox couple. Enhanced electrocatalytic activity is marked by higher peak current densities and a smaller ΔE_p

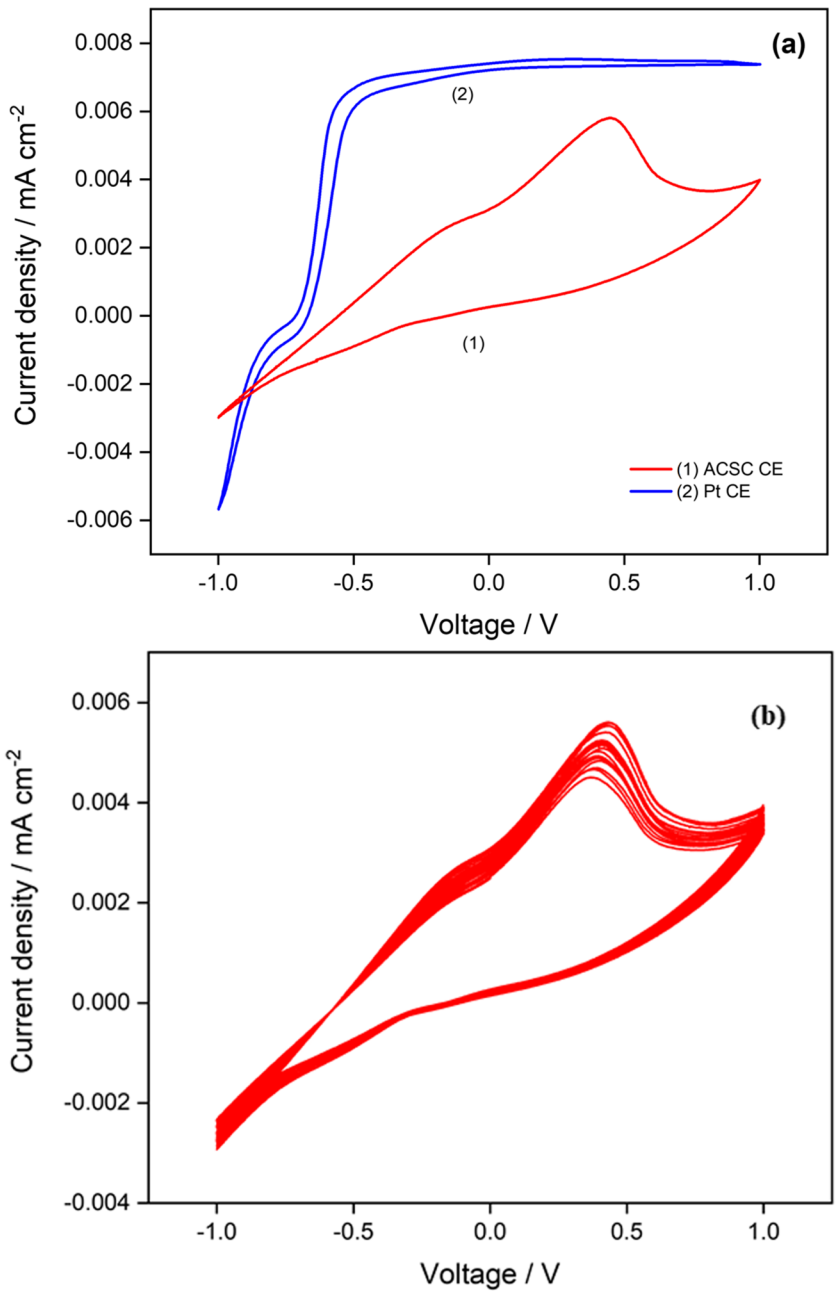

Fig. 9 **a** Cyclic voltammograms of ACSC CE and Pt CEs and **b** ACSC CE for 20 cycles at a scan rate of 20 $mVs.^{-1}$

value. Moreover, the electrical conductivity of the CE is closely associated with the peak currents for oxidation and reduction [37]. While the Pt CE shows no significant peaks, the ACSC CEs exhibit clear J_{ox} and J_{red} peaks, with 2.36×10^{-3} mA cm^{-2} and 1.45×10^{-4} mA cm^{-2}, respectively, along with a ΔE_p value of 0.096 V. These findings indicate that ACSC CEs demonstrate superior electrocatalytic activity compared to Pt CEs, especially in the context of quantum dot–sensitized solar cells (QDSSCs). This is mainly due to the superior electrocatalytic activity of ACSC due to its porous structure and high density of active sites, which enables efficient redox reactions of the polysulfide electrolyte. On the other hand, the performance of Pt in polysulfide electrolytes is hindered by the adsorption of sulfur species on its surface, which blocks active sites and suppresses redox activity.

The electrochemical stability of the ACSC CE was evaluated through preliminary investigations by recording cyclic voltammograms over 20 consecutive cycles at a scan rate of 20 mV s^{-1}, as illustrated in Fig. 9b. The cyclic voltammograms exhibit negligible shifts in peak positions, indicating that the ACSC counter electrode demonstrates potential as an effective counter electrode for use in QDSSCs.

Electrochemical impedance analysis of counter electrodes by EIS

EIS tests were also performed on two different counter electrodes using symmetrical dummy cells constructed with two identical electrodes, each having an active area of 1.00 cm^2, to investigate the charge transfer process at the counter electrode/electrolyte interface.

The associated Randles circuit used to fit the Nyquist curves is displayed in the inset of the graph, while the resulting Nyquist plots can be found in Fig. 10. An expanded version of the plot is included in the inset to enhance clarity for the Nyquist plot of the ACSC CE. The standard Nyquist plot features a distinct semicircle with a half curve, which indicates the charge transfer resistance (R_{CT}) and the corresponding constant-phase element at the electrolyte/electrode interface. The remaining portion of the curve represents the Nernst diffusion impedance of the electrolyte. The series resistance (R_S), which primarily consists of the bulk resistance of the CE material, the resistance of the FTO layer, and the constant resistance at the FTO/electrode interface, is incorporated into the equivalent circuit and can be determined from the intercept on the real axis. This study mainly concentrates on the R_S and R_{CT} values associated with the ACSC CE and Pt CE, as outlined in Table 4.

Table 4 Electrochemical parameters of the two counter electrodes extracted from both EIS measurements and Tafel plot results

Counter electrode	R_S (Ω)	R_{CT} (Ω)	log J_o/mA cm^{-2}	log J_{lim}/mA cm^{-2}
ACSC	25.59	2.65	1.33	1.90
Pt	2.37	333.52	1.27	1.35

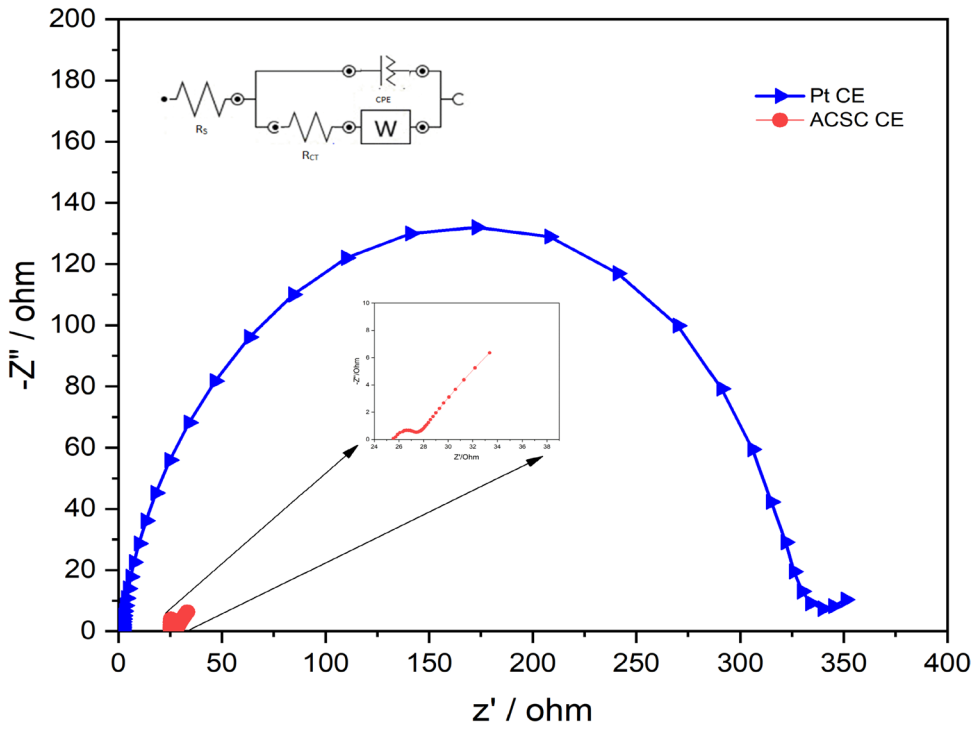

Fig. 10 Nyquist plots for symmetric cells fabricated with (1) ACSC CE and (2) Pt CE

As shown in Table 4, the R_{CT} value for the ACSC CE is 2.65 Ω, considerably lower than that of the Pt CE. This reduced R_{CT} suggests that the ACSC CE facilitates electron transfer dynamics, leading to better photovoltaic performance of the QDSSCs compared to the Pt CE. However, the R_S value for ACSC is 25.59 Ω, which is significantly higher than that of the Pt CE, quite likely due to the poor interface attachment between ACSC powder and FTO and the excellent electronic conductivity of Pt.

Tafel analysis

Figure 11 displays the Tafel curves, where logarithmic current density is plotted against applied voltage. The Tafel curve is primarily divided into three regions: the polarization zone, the Tafel zone, and the diffusion zone. The exchange current density (J_o) and the limiting diffusion current density (J_{lim}), both associated with the polarization zone, are directly related to the electrocatalytic activity of the counter electrode [37]. J_o is particularly tied to the catalytic activity of the CE and is used to evaluate the ability of the CEs to reduce the polysulfide electrolyte, with a higher J_o value indicating better catalytic activity for electrolyte reduction [38]. The limiting diffusion current density (J_{lim}), determined by the intersection of the cathodic branch with the *Y*-axis, assesses the diffusion performance of the redox couples. J_o is calculated from the polarization region, whereas J_{lim} is derived from the diffusion region [39]. The exchange current density can be directly determined by extrapolating the linear region of the Tafel plot to $\eta = 0$, which corresponds to the equilibrium potential where the current density equals J_o.

Table 4 summarizes the J_o and J_{lim} values for ACSC CEs and Pt CEs. As shown, the J_o values for ACSC CEs and Pt CEs are 1.33 mA cm^{-2} and 1.27 mA cm^{-2}, respectively. These values are consistent with the relationship between R_{CT} and J_o as expressed by Eq. (2).

$$J_o = \frac{RT}{nFR_{CT}} \tag{2}$$

where R represents the gas constant, T denotes the absolute temperature, and R_{CT} is the charge transfer resistance extracted from the EIS data. According to the equation, J_o is inversely related to R_{CT}. As a result, the findings from the EIS measurements are in strong agreement with those obtained from the Tafel plot. Specifically, the higher J_o and J_{lim} values correspond to the lower resistance observed in the EIS measurements for the counter electrodes. These increased values of J_o and J_{lim} may be attributed to the larger specific surface area of the ACSC CE, which enhances the electro-catalytic activity of the counter electrode towards the polysulfide electrolyte.

Table 5 presents a comparison of the efficiencies of various CdS QDSSCs fabricated with carbon-based counter electrodes, as reported by different research groups in the

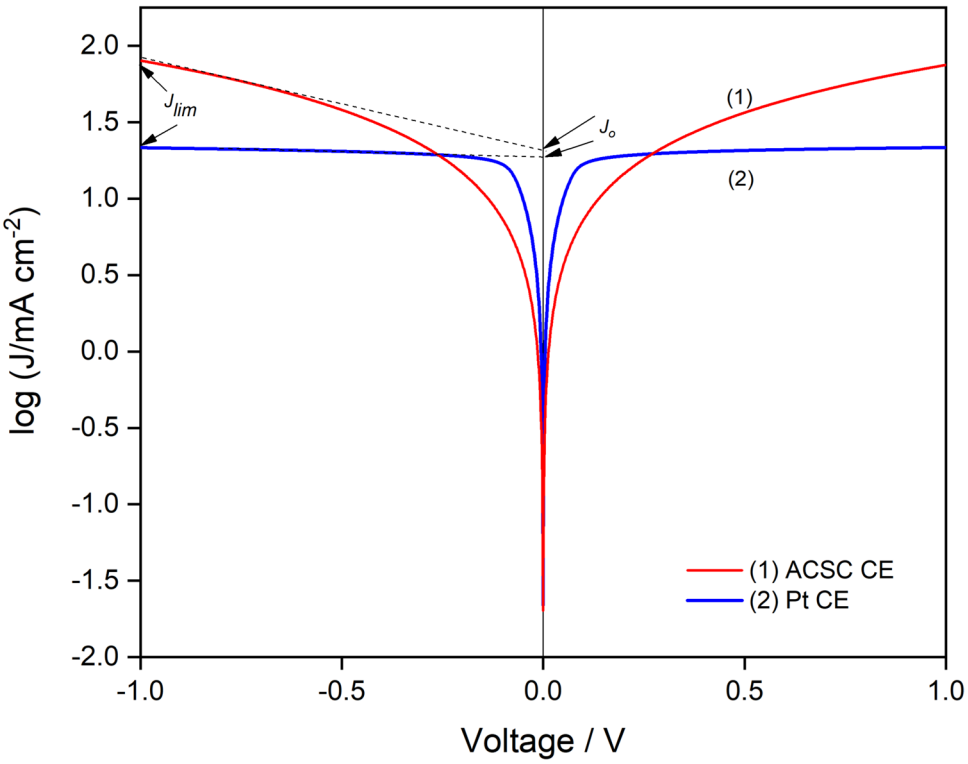

Fig. 11 Tafel polarization curves for symmetric cells with (1) ACSC CE and (2) Pt CE

Table 5 Comparison of the performance of carbon-based counter electrodes reported in the literature with the present work (listed in the final row)

Material	Binder	Preparation	Sinter temperature	Efficiency (%)	Redox electrolyte	Ref
Carbon black/CuS	Ethyl cellulose	Spin coating	Dried at 60 °C 15 min	1.3	Polysulfide	[40]
Black carbon soot	-	Holding substrate on top of the flame	-	0.38	Polysulfide	[41]
Activated carbon/conductive carbon black	PVDF	Screen printing	100 °C overnight	1.47	Polysulfide	[42, 43, 44]
HCMSC	Nafion	Doctor blade	400 °C/15 min	1.08	Polysulfide	[8]
Activated coconut shell charcoal	PVP	Spray	350 °C/20 min	2.93	polysulfide	This work

literature, along with their preparation methods, sintering temperatures, and the type of electrolyte used. The results from the current study, based on ACSC CE, are listed in the final row. To the best of our knowledge, there have been no prior reports on the performance of QDSSCs made with this innovative and cost-effective ACSC counter electrode.

Conclusion

A straightforward method was successfully applied to produce activated charcoal from coconut shell charcoal and fabricate ACSC-based counter electrodes for use in CdS QDSSCs. A cost-effective and simple spray technique was used to create a counter electrode with a nanoporous structure, offering an increased specific surface area, improved electrocatalytic activity, and enhanced electronic conductivity. This nanostructured CE also appears to provide more effective interconnecting pathways for efficient electron transfer dynamics, along with improved electrocatalytic performance for the reduction of the polysulfide electrolyte at the CE. In comparison to the 1.26% efficiency of Pt CE-based QDSSCs, the novel ACSC CE-based QDSSCs achieved a significantly higher power conversion efficiency of 2.93%, with an enhanced short-circuit photocurrent density (J_{sc}) of 13.62 mA cm^{-2}. The ACSC CE showed excellent electrocatalytic activity towards the reduction of polysulfide electrolyte at the electrolyte/CE interface, as confirmed. The results presented here highlight the novel ACSC CE as a promising, low-cost alternative for fabricating high-performance QDSSCs.

Acknowledgements Authors gratefully acknowledge the financial support provided by the Swedish Research Council, Dnr. 2021-04889, under the Swedish Research Links Network grant for collaborative research on solar cells between Sweden, Sri Lanka, India and Nigeria.

Author contribution M.A.K.L. Dissanayake: conceptualization, supervision, checking data, editing manuscript; A.K. Karunaratne: investigation, data curation, methodology, formal analysis, writing-original draft; G.K.R. Senadeera: conceptualization, supervision, checking data, editing manuscript; T.M.W.J. Bandara: supervision, editing; G.R.A. Kumara: resources, supervision of activated charcoal part; A.D.T. Medagedara: resources, experimental activated charcoal part; J.M.K.W. Kumari: supervision, checking data, editing manuscript; I. Albinsson: resources, guidance, editing; B-E. Mellander: resources, guidance, editing; M. Furlani: resources, guidance, editing; N. B. Chaure: resources, guidance, editing; O. I. Olusola: resources, guidance, editing.

Data availability No datasets were generated or analysed during the current study.

Declarations

Competing interests The authors declare no competing interests.

References

1. Barnham K, Duggan G (1990) A new approach to high-efficiency multi-band-gap solar cells. J Appl Phys 67(7):3490–3493. https://doi.org/10.1063/1.345339
2. Nozik AJ (2002) Quantum dot solar cells. Physica E 14(1–2):115–120. https://doi.org/10.1016/S1386-9477(02)00374-0
3. Song H, Lin Y, Zhou M, Rao H, Pan Z, Zhong X (2021) Zn-Cu-In-S-Se Quinary "Green" Alloyed Quantum-Dot-Sensitized Solar Cells with a Certified Efficiency of 144%. Angewandte Chemie Int Ed 60(11):6137–44. https://doi.org/10.1016/j.solener.2018.06.095
4. Kumar PN, Kolay A, Kumar SK, Patra P, Aphale A, Srivastava AK, Deepa M (2016) Counter electrode impact on quantum dot solar cell efficiencies. ACS Appl Mater Interfaces 8(41):27688–27700. https://doi.org/10.1021/acsami.6b08921
5. Chen H, Zhu L, Liu H, Li W (2014) Efficient iron sulfide counter electrode for quantum dots-sensitized solar cells. J Power Sources 245:406–410. https://doi.org/10.1016/j.jpowsour.2013.06.004
6. Yeh M-H, Lee C-P, Chou C-Y, Lin L-Y, Wei H-Y, Chu C-W, Vittal R, Ho K-C (2011) Conducting polymer-based counter electrode for a quantum-dot-sensitized solar cell (QDSSC) with a polysulfide electrolyte. Electrochim Acta 57:277–284. https://doi.org/10.1155/2014/491912
7. Elibol E (2020) Effects of different counter electrodes on performance of CdSeTe alloy QDSSC. Sol Energy 197:519–526. https://doi.org/10.1016/j.solener.2020.01.035
8. Paul GS, Kim JH, Kim M-S, Do K, Ko J, Yu J-S (2012) Different hierarchical nanostructured carbons as counter electrodes for CdS quantum dot solar cells. ACS Appl Mater Interfaces 4(1):375–381. https://doi.org/10.1021/am201452s

9. Prasad AK, Jo I-R, Kang S-H, Ahn K-S (2021) Novel method for synthesis of reduced graphene oxide–Cu2S and its application as a counter electrode in quantum-dot-sensitized solar cells. Appl Surf Sci 564:150393. https://doi.org/10.1016/j.apsusc.2021.150393
10. Sun J-K, Jiang Y, Zhong X, Hu J-S, Wan L-J (2017) Three-dimensional nanostructured electrodes for efficient quantum-dot-sensitized solar cells. Nano Energy 32:130–156. https://doi.org/10.1016/j.rechem.2022.100291
11. Hwang I, Yong K (2015) Counter electrodes for quantum-dot-sensitized solar cells. ChemElectroChem 2(5):634–653. https://doi.org/10.1002/celc.201402405
12. Kumarasinghe K, Kumara G, Rajapakse R, Liyanage D, Tennakone K (2019) Activated coconut shell charcoal based counter electrode for dye-sensitized solar cells. Org Electron 71:93–97. https://doi.org/10.1016/j.orgel.2019.05.009
13. Keppetipola NM, Dissanayake M, Dissanayake P, Karunarathne B, Dourges MA, Talaga D, Servant L, Olivier C, Toupance T, Uchida S, Tennakone K (2021) Graphite-type activated carbon from coconut shell: a natural source for eco-friendly non-volatile storage devices. RSC Adv 11(5):2854–65. https://doi.org/10.1039/d0ra09182k
14. Lobato-Peralta DR, Okoye PU, Alegre C (2024) A review on carbon materials for electrochemical energy storage applications: state of the art, implementation, and synergy with metallic compounds for supercapacitor and battery electrodes. J Power Sources 617:235140. https://doi.org/10.1016/j.jpowsour.2024.235140
15. Mohammad-Khah A, Ansari R (2009) Activated charcoal: preparation, characterization and applications: a review article. Int J Chem Tech Res 1(4):859–864
16. Dissanayake M, Jaseetharan T, Senadeera G, Mellander B, Albinsson I, Furlani M, Kumari J (2021) Solid-state solar cells co-sensitized with PbS/CdS quantum dots and N719 dye and based on solid polymer electrolyte with binary cations and nanofillers. J Photochem Photobiol, A 405:112915. https://doi.org/10.1016/j.jphotochem.2020.112915
17. Ali MH, Haque MD, Hossain MF, Hossain MM, Rahman MF, Islam T, Md AZ (2024) Effect of Triton X-100 surfactant on structural, morphological, and optical properties of ZnS thin films deposited by spin coating method. J Sol-Gel Sci Technol 2:560–566. https://doi.org/10.1007/s10971-024-06368-y
18. Dissanayake M, Liyanage T, Jaseetharan T, Senadeera G, Dassanayake B (2020) Effect of PbS quantum dot-doped polysulfide nanofiber gel polymer electrolyte on efficiency enhancement in CdS quantum dot-sensitized TiO_2 solar cells. Electrochim Acta 347:136311. https://doi.org/10.1016/j.electacta.2020.136311
19. Medagedara A, Waduge N, Bandara T, Wimalasena I, Dissanayake M, Tennakone K, Rajapakse R, Rupasinghe C, Kumara G (2022) Triethylammonium thiocyanate ionic liquid electrolyte-based supercapacitor fabricated using coconut shell-derived electronically conducting activated charcoal electrode material. J Energy Stor 55:105628. https://doi.org/10.1016/j.est.2022.105628
20. Dissanayake M, Umair K, Senadeera G, Jaseetharan T, Weerasinghe A, Wijayasinghe H (2022) Plasmonic gold nanoparticle incorporated MgO-coated SnO_2 photoanode for efficiency enhancement in dye-sensitized solar cells. Sol Energy 233:363–377. https://doi.org/10.1016/j.solener.2022.01.038
21. Sujiono EH, Zabrian D, Zharvan V, Humairah N (2022) Fabrication and characterization of coconut shell activated carbon using variation chemical activation for wastewater treatment application. Res Chem 4:100291. https://doi.org/10.1016/j.rechem.2022.100291
22. Zhao Y, Cho C-W, Cui L, Wei W, Cai J, Wu G, Yun Y-S (2019) Adsorptive removal of endocrine-disrupting compounds and a pharmaceutical using activated charcoal from aqueous solution: kinetics, equilibrium, and mechanism studies. Environ Sci Pollut Res 26:33897–33905. https://doi.org/10.1007/s11356-018-2617-7
23. Sujiono EH, Zabrian D, Zharvan V, Humairah NA (2022) Fabrication and characterization of coconut shell activated carbon using variation chemical activation for wastewater treatment application. Res Chem 4:100291. https://doi.org/10.1016/j.rechem.2022.100291
24. Xie Z, Guan W, Ji F, Song Z, Zhao Y (2014) Production of biologically activated carbon from orange peel and landfill leachate subsequent treatment technology. J Chem 2014(1):491912
25. Nishikawa T, Gotoh H, Nishimura T, Kawasumi T, Horie Y, Tsubokawa N, Iwata T (2018) Effect of graphite structures on the productivity and quality of few-layer graphene in liquid-phase exfoliation. J Mater Sci 53(62):6217. https://doi.org/10.1007/s10853-018-2538-3
26. Senadeera GKR, Rasnayake RMSS, Kumari JMKW, Sandunika PU, Dissanayaka MAKL, Jayathilake DLN, Jaseetharan T, Ekanayake P (2024) Novel platinum-free counter-electrode with PEDOT:PSS-treated graphite/activated carbon for efficient dye-sensitized solar cells. Ionics. https://doi.org/10.1007/s11581-024-05872-z
27. Wu J, Lan Z, Lin J, Huang M, Huang Y, Fan L, Luo G, Lin Y, Xie Y, Wei Y (2017) Counter electrodes in dye-sensitized solar cells. Chem Soc Rev 46(19):5975–6023. https://doi.org/10.1039/C6CS00752J
28. Raj CJ, Prabakar K, Savariraj AD, Kim H-J (2013) Surface reinforced platinum counter electrode for quantum dots sensitized solar cells. Electrochim Acta 103:231–236
29. Li T-L, Lee Y-L, Teng H (2012) High-performance quantum dot-sensitized solar cells based on sensitization with CuInS2 quantum dots/CdS heterostructure. Energy Environ Sci 5(1):5315–5324. https://doi.org/10.1039/C1EE02253A
30. Ghosh D, Halder G, Sahasrabudhe A, Bhattacharyya S (2016) A microwave synthesized Cu x S and graphene oxide nanoribbon composite as a highly efficient counter electrode for quantum dot sensitized solar cells. Nanoscale 8(20):10632–10641. https://doi.org/10.1039/C6NR01161F
31. Meng K, Chen G, Thampi KR (2015) Metal chalcogenides as counter electrode materials in quantum dot sensitized solar cells: a perspective. J Mater Chem A 3(46):23074–23089. https://doi.org/10.1039/C5TA05071E
32. Kusuma J, Balakrishna RG (2018) A review on electrical characterization techniques performed to study the device performance of quantum dot sensitized solar cells. Sol Energy 159:682–696. https://doi.org/10.1016/j.solener.2017.11.037
33. Singh N, Murugadoss V, Nemala S, Mallick S, Angaiah S (2018) Cu2ZnSnSe4 QDs sensitized electrospun porous TiO2 nanofibers as photoanode for high performance QDSC. Sol Energy 171:571–579. https://doi.org/10.1016/j.solener.2018.06.095
34. Du Z, Pan Z, Fabregat-Santiago F, Zhao K, Long D, Zhang H, Zhao Y, Zhong X, Yu J-S, Bisquert J (2016) Carbon counter electrode-based quantum dot sensitized solar cells with certified efficiency exceeding 11%. J Phys Chem Lett 7(16):3302–3308. https://doi.org/10.1021/acs.jpclett.6b01356
35 Liyanage TS, Jaseetharan T, Sandamali WI, Dissanayake MA, Perera VP, Rajendra JC, Karthikeyan N, Senadeera GK (2021) through incorporation of chemically deposited compact SnO. Ceylon J Sci 50(3):243–8. https://doi.org/10.4038/cjs.v50i3.7905
36. Ren F, Li S, He C (2015) Electrolyte for quantum dot-sensitized solar cells assessed with cyclic voltammetry. Sci China Mater 58:490–495. https://doi.org/10.1016/j.electacta.2013.04.016
37 Saliba M, Stolterfoht M, Wolff CM, Neher D, Abate A (2018) Measuring aging stability of perovskite solar cells. Joule 2(6):1019–24. https://doi.org/10.1016/j.joule.2018.05.005
38. Xu T, Kong D, Tang H, Qin X, Li X, Gurung A, Kou K, Chen L, Qiao Q, Huang W (2020) Transparent MoS2/PEDOT composite counter electrodes for bifacial dye-sensitized solar cells.

ACS Omega 5(15):8687–8696. https://doi.org/10.1021/acsomega.0c00175
39. Dissanayake M, Kumari J, Senadeera G, Anwar H (2021) Low cost, platinum free counter electrode with reduced graphene oxide and polyaniline embedded SnO2 for efficient dye sensitized solar cells. Sol Energy 230:151–165. https://doi.org/10.1016/j.solener.2021.10.022
40. Monika S, Mahalakshmi M, Veerathangam K, Senthil Pandian M, Ramasamy P (2022) Conductive carbon black/CuS composite counter electrode for the enhanced photovoltaic performance of CdS quantum dot sensitized solar cells. Appl Phys A 128(3):228. https://doi.org/10.1007/s00339-022-05356-9
41. Sajjad S, Sayyad MH, Khan N, Manzoor T, Nasr N, Toor RA, Shah SAA, Guo Z (2021) Comparative photovoltaic and impedance spectroscopic study on carbon counter electrode based CdS quantum dot sensitized solar cell using polysulfide and iodide/triiodide as redox liquid electrolytes. Mater Sci Eng, B 273:115437. https://doi.org/10.1016/j.mseb.2021.115437
42. Zhang Q, Zhang Y, Huang S, Huang X, Luo Y, Meng Q, Li D (2010) Application of carbon counterelectrode on CdS quantum dot-sensitized solar cells (QDSSCs). Electrochem Commun 12(2):327–330. https://doi.org/10.1016/j.elecom.2009.12.032
43. Riaz R, Ali M, Maiyalagan T, Arbab AA, Anjum AS, Lee S, Ko MJ, Jeong SH (2020) Activated charcoal and reduced graphene sheets composite structure for highly electro-catalytically active counter electrode material and water treatment. Int J Hydrogen Energy 45(13):7751–7763. https://doi.org/10.1016/j.ijhydene.2019.06.138
44. Seehra MS, Pavlovic AS, Ebrahimi F (2016) Correlation between X-ray diffraction and Raman spectra of 16 commercial graphene-based materials and their resulting classification. Carbon 111:380–386. https://doi.org/10.1016/j.carbon.2016.10.010

Authors and Affiliations

M. A. K. L. Dissanayake[1,2] · A. K. Karunaratne[1,2] · G. K. R. Senadeera[1,3] · T. M. W. J. Bandara[2,4] · G. R. A. Kumara[1] · A. D. T. Medagedara[1] · J. M. K. W. Kumari[1] · I. Albinsson[5] · B.-E. Mellander[6] · M. Furlani[6] · N. B. Chaure[7] · O. I. Olusola[8]

✉ M. A. K. L. Dissanayake
makldis@yahoo.com

✉ I. Albinsson
ialbin@physics.gu.se

A. K. Karunaratne
kaushalyawin93@gmail.com

G. K. R. Senadeera
gkrsena@yahoo.com

T. M. W. J. Bandara
awijendr@yahoo.com

G. R. A. Kumara
kumara.as@nifs.ac.lk

A. D. T. Medagedara
asiri.me@nifs.ac.lk

J. M. K. W. Kumari
kalpani.ku@nifs.ac.lk

B.-E. Mellander
f5xrk@chalmers.se

M. Furlani
f6bmauri@chalmers.se

N. B. Chaure
nchaure.uop@gmail.com

O. I. Olusola
olajideibk@yahoo.com

[1] National Institute of Fundamental Studies, Kandy 20000, Sri Lanka

[2] Postgraduate Institute of Science, University of Peradeniya, Peradeniya 20400, Sri Lanka

[3] Department of Physics, The Open University of Sri Lanka, Nawala 10250, Nugegoda, Sri Lanka

[4] Department of Physics, University of Peradeniya, Peradeniya 20400, Sri Lanka

[5] Department of Physics, University of Gothenburg, 41296 Gothenburg, Sweden

[6] Department of Applied Physics, Chalmers University of Technology, 41296 Gothenburg, Sweden

[7] Department of Physics, Savitribai Phule Pune University, Pune-411007, India

[8] Department of Physics, The Federal University of Technology Akure, Akure 340271, Nigeria